# Modeling the gravitational effects of ocean tide loading at coastal stations in the China earthquake gravity network based on GOTL software



**Author(s):**
Zhu, Chuandong; Pang, Liuqing; Sheng, Didi; Huang, Jialiang; Li, Jinwu

**Publication date:**
2023

**Permanent link:**
https://doi.org/10.3929/ethz-b-000581686



**Originally published in:**
Journal of Applied Geodesy 17(1), https://doi.org/10.1515/jag-2022-0023

Chuandong Zhu*, Liuqing Pang, Didi Sheng, Jialiang Huang and Jinwu Li

# Modeling the gravitational effects of ocean tide loading at coastal stations in the China earthquake gravity network based on GOTL software

https://doi.org/10.1515/jag-2022-0023
Received July 27, 2022; accepted October 15, 2022;
published online November 3, 2022

**Abstract:** The gravitational effects of ocean tide loading, which are one of the main factors affecting gravity measurements, consist of three components: (1) direct attraction from the tidal water masses, (2) radial displacement of the observing station due to the tidal load, and (3) internal redistribution of masses due to crustal deformation. In this study, software for gravitational effects of ocean tide loading was developed by evaluating a convolution integral between the ocean tide model and Green's functions that describe the response of the Earth to tide loading. The effects of three-dimensional station coordinates, computational grid patterns, ocean tide models, Green's functions, coastline, and local tide gauge were comprehensively considered in the programming process. Using a larger number of high-precision coastlines, ocean tide models, and Green's functions, the reliability and applicability of the software were analyzed at coastal stations in the China Earthquake Gravity Network. The software can provide the amplitude and phase for ocean tide loading and produce a predicted gravity time series. The results can effectively reveal the variation characteristics of ocean tide loading in space and time. The computational gravitational effects of ocean tide loading were compared and analyzed for different ocean tide models and Green's functions. The results show that different ocean tide models and Green's functions have certain effects on the calculated values of loading gravity effects. Furthermore, a higher-precision local ocean tide model, digital elevation model, and local tidal gauge record can be further imported into our software to improve the accuracy of loading gravity effects in the global and local zones. The software is easy to operate and can provide a comprehensive platform for correcting the gravitational effects of ocean tide loading at stations in the China Earthquake Gravity Network.

**Keywords:** GOTL software; gravitational effect; green's functions; ocean tide loading; ocean tide model.

## 1 Introduction

Following the Xingtai earthquake in the 1960s, terrestrial gravity measurements in China were gradually conducted to practice earthquake prediction [1, 2]. After decades of construction, the China Earthquake Gravity Network (CEGN), composed of continuous (86 stations) and mobile gravity observations (105 absolute gravity points and approximately 4,000 relative gravity points), has been formed. At present, there are 92 sets of instruments at continuous gravity stations, including 8 GS15, 18 DZW, 3 TGR, 61 PET & gPhone, and 2 GWR iGrav superconducting gravimeters [3–5]. The absolute gravity points are observed with FG5 and A10 absolute gravimeters, and the relative gravity points are measured with LCR-G, CG5/CG6, and Burris relative gravimeters. The accuracy of the continuous and mobile gravity observations of the CEGN can reach 0.1–1 μGal and 10 μGal (1 μGal equals $10^{-8}$ m/s$^2$), respectively. The network can effectively obtain gravity changes in mainland China, provide basic data for seismic research, and be used for maintaining gravity datum in China.

To obtain the geophysical and geodynamical variations in gravimeter recordings of the CEGN, the tidal signals, including solid earth tide and ocean tide loading effects, must be corrected [6, 7]. Ocean tide loading is the deformation of the Earth's crust due to the load of the ocean tides caused by gravitational forces from the celestial bodies. The gravitational ocean tide loading effect has three constituent parts: gravitational change caused

*Corresponding author: Chuandong Zhu, The First Monitoring and Application Center, CEA, Tianjin, China,
E-mail: zhuchuandong2006@sina.com. https://orcid.org/0000-0003-2499-2561
Liuqing Pang, Didi Sheng and Jialiang Huang, The First Monitoring and Application Center, CEA, Tianjin, China
Jinwu Li, The First Monitoring and Application Center, CEA, Tianjin, China; and ETH Zurich, 8092 Zurich, Switzerland

by (1) direct attraction from the tidal water masses, (2) radial displacement of the observing station due to the tidal load, and (3) internal redistribution of Earth's masses due to crustal deformation [3]. Farrell [8] developed a method to compute the ocean tide loading effects that involve performing calculations through the convolution between an ocean tide model and appropriate Green's functions.

The accuracy of ocean tide loading effects greatly depends on the accuracy of the ocean tide model. With the improvements in hydrodynamic models of tidal propagation that assimilate available tide gauges and satellite altimetry and direct empirically produced models from satellite altimetry, tidal research groups have published a series of global and local ocean tide models, including Schwiderski [9, 10], FES [11], CSR [12], GOT [13], NAO [14], TPXO [15], EOT [16], DTU [17], OSU [18], and HAMTIDEOSU [19]. Current ocean tide models have strong consistency in the deep ocean and can reach centimeter-level accuracy [20–22]. The main differences between tidal models appear in the coastal and continental shelf areas. These results suggest the importance of detailed modeling of the local ocean tide loading effects when correcting terrestrial gravity measurements at coastal stations. Moreover, the accuracy of ocean tide loading effects is determined by the Green's functions, which are the linear combination of dimensionless load Love numbers. The load Love numbers are known as load deformation coefficients, describing the response of the Earth to the surface mass load. For a spherically symmetric nonrotating elastic isotropic (SNREI) Earth model, the fundamental methodology related to computations of the load Love numbers and Green's functions can be found in previous works [23–25], which are applied to the numerical calculation for elastic Earth models PREM, ak135, iasp91, and modified models by refined crustal structure [26].

In this study, we developed a correction software, GOTL, for gravitational effects of ocean tide loading. Although there are several independent software packages, such as SPOTL [27–29], Bos–Scherneck [30], GOTIC2 [31], SGOTL [32], and LoadDef [33], our purpose here was to provide an easily operatable and comprehensive platform for correcting terrestrial gravity measurements in the CEGN. The gravitational effects of ocean tide loading were assessed at five selected coastal gravity stations in the CEGN. As shown in Figure 1, these five stations, including Qiongzhong, Pingtan, Shanghai, Qingdao, Jixian, are located in four major sea areas of China. The impacts of different coastlines, ocean tide models, and Green's functions were further analyzed and discussed.

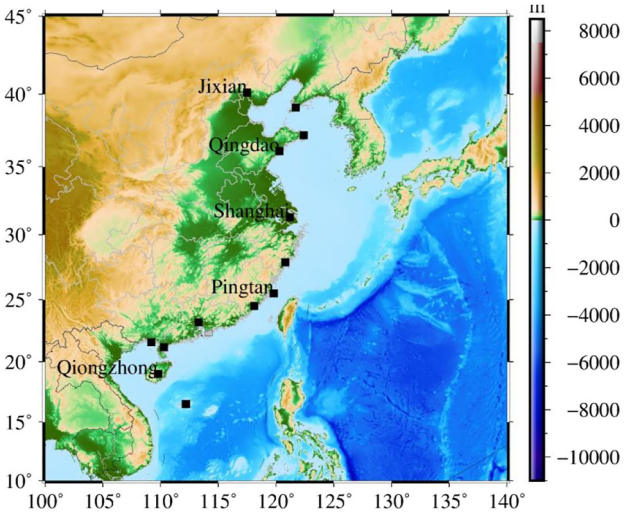


**Figure 1:** Distribution of CEGN coastal gravity stations. These stations are observed by high-precision continuous, absolute, and relative gravimeters.

## 2 Data and data processing

### 2.1 Basic formulation

The ocean tide loading effects at each station on the surface of the Earth can be computed by convolving Green's functions with an ocean tide distribution model [8, 34, 35]. For a particular tidal constituent $n$, the ocean tide loading effects $L_n$ at latitude $\phi$ and longitude $\lambda$ is given by the convolution integral:

$$L_n(\varphi, \lambda) = \rho_w \iint_{\Omega} H(\varphi', \lambda') G(\psi) \mathrm{d}s \tag{1}$$

where $\rho_w$ is the density of seawater, $H$ is the elevation of the ocean tide for a given tidal constituent over surface area d$s$ at latitude $\varphi'$ and longitude $\lambda'$. $\Omega$ is the region of integration, i.e., the global ocean area. $G(\psi)$ is the Green's functions, which can characterize the gravity change using a function of the angular distance $\psi$ between the observation point and a point mass load. For the convolution integral in formula (1), its numerical evaluation is then given by [36, 37]:

$$L_n(\varphi, \lambda) = \rho_w \sum_{i=0}^{N} H_i(\varphi', \lambda') G(\psi_i) \mathrm{d}s_i \tag{2}$$

where the global ocean area is divided into a set of grids, and $N$ is the corresponding total number of grids.

With the above basic formulation, we further developed a software to compute the gravitational effects of

ocean tide loading based on MATLAB. As shown in Figure 2, all the parameters related to station coordinates, computational grid patterns, ocean tide models, Green's functions, coastline, and local tide gauge can be set in the graphical user interface.

## 2.2 Computational grid patterns

In this study, the coastline information was collected from the Global Self-consistent, Hierarchical, High-resolution Geography Database (GSHHG) in full resolution and shuttle radar topographic mission (SRTM) digital elevation model (DEM) to extract the global and regional land–ocean distribution, respectively [38–40].

As shown in Figure 3, computational grid patterns of five regions describing land–ocean distribution were provided to compute loading gravity effects in the global and local zone. The boundary of the computational grid patterns and its associated grid size can be appropriately set according to the angular distance in formula (2). Finer-scale grids should be set for the nearer regions adjacent to the calculated point where the variation of Green's functions is large in terms of angular distance. Based on the above parameter settings, the ocean surface height and Green's functions concentrated at the associated center of grids were interpolated using linear and cubic interpolation.

## 2.3 Ocean tide models

For a single tidal constituent with frequency $\omega$, global ocean surface height in space and time can be predicted with amplitude $h$ and Greenwich phase $\delta$ provided by the ocean tide models:

$$\begin{aligned} H_n(\varphi, \lambda, t) &= h\cos(\omega t + \chi - \delta) \\ &= H_c\cos(\omega t + \chi) + H_s\sin(\omega t + \chi) \end{aligned} \quad (3)$$

where $\chi$ is the corresponding astronomical argument. To force mass conservation of the ocean tide, we removed a uniform sheet of water from $H_c$ and $H_s$ [41, 42]:

$$H_c^* = H_c - \frac{\sum_i H_c S_i}{\sum_i S_i}, H_s^* = H_s - \frac{\sum_i H_s S_i}{\sum_i S_i} \quad (4)$$

where $S_i$ is the oceanic grid area.

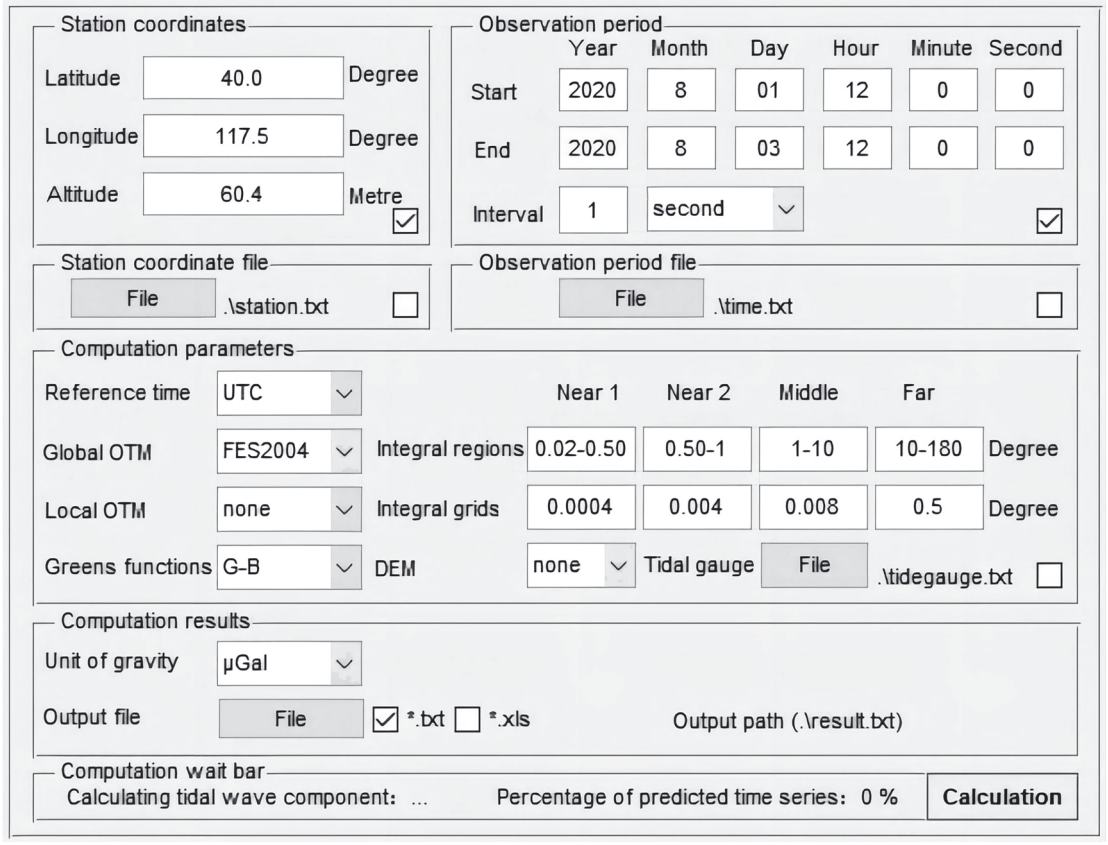


**Figure 2:** The interface of software for computing the gravitational effects of ocean tide loading.

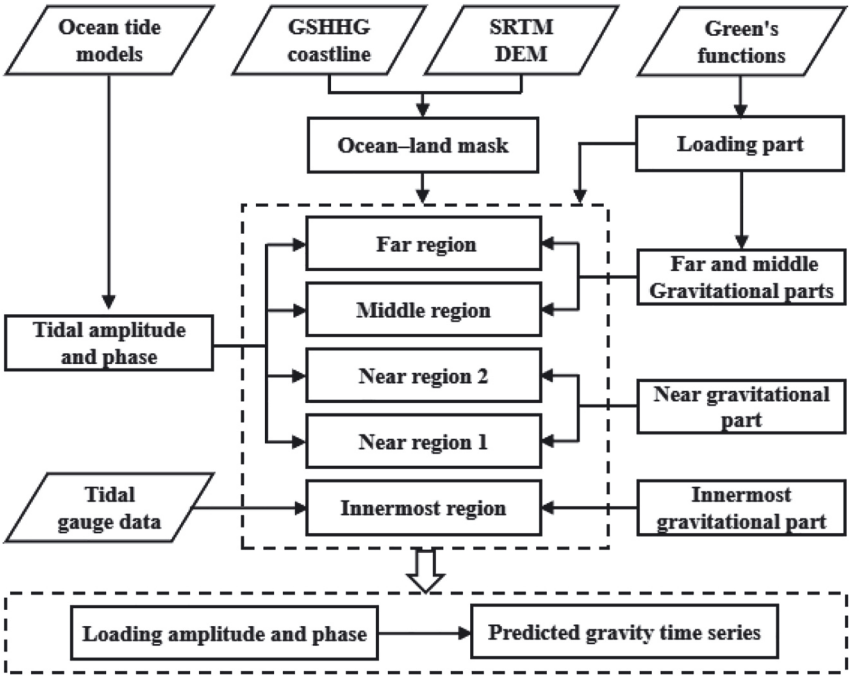


**Figure 3:** The calculation flow chart of gravitational effects of ocean tide loading in GOTL.

As shown in Figure 2, our software can provide a series of global and local ocean tide models, including NAO, TPXO, FES, EOT, DTU, and CSR. These ocean tide models can provide the amplitudes and Greenwich phases for 11 main constituents, i.e., semi-diurnal harmonics M2, S2, N2, and K2; diurnal harmonics K1, O1, P1, and Q1; and long-period harmonics Mf, Mm, and Ssa, which account for more than 95% of the tidal signal [43, 44].

## 2.4 Green's functions

In this study, the computation of Green's functions for gravity was divided into the loading and gravitational parts. The loading part consists of radial displacement of the observing station due to the tidal load and internal redistribution of Earth's masses due to crustal deformation. For the computational grid patterns of five regions in Figure 3, the expression of the loading part to a point mass load is given as [8]:

$$G_g^l(\psi) = \frac{g_0}{m_e}\sum_{n=0}^{\infty}\left[2h'_n - (n+1)k'_n\right]P_n\cos(\psi) \qquad (5)$$

where $g_0$ is the mean surface gravity, $m_e$ is the total mass of the Earth, $P_n$ is the Lengendre function of degree $n$, $h'_n$ and $K'_n$ is the load Love number. As shown in Figure 2, there are six potential Green's functions, which are precomputed based on the Gutenberg–Bullen [8], 1066A [45], PREM, ak135, iasp91, and modified Earth models by refined crustal structure [26]. These Green's functions were all given in the Center of Earth Frame, as our study is aimed at observations on the Earth.

For the computational grid patterns of near (near 1 and 2) and middle-far regions in Figure 3, the expression of the gravitational part to a point mass load is given as [8]:

$$G_g^g(\psi) = \begin{cases} G\dfrac{\left[d^2 + (R+h_s)^2 - R^2\right]}{2d^3(R+h_s)}, \langle \text{In near regions} \rangle \\ \dfrac{g_0}{4m_e\,\sin(\psi/2)}, \langle \text{In middle and far regions} \rangle \end{cases} \qquad (6)$$

where $G$ is the gravitational constant, $R$ is the radius of the Earth, $d$ is the distance between the observation point and a point mass load, $h_s$ is the height of the observation station, and its reference surface is the mean sea level. In comparison, the expression in near regions can comprehensively account for the effect of the topography [46].

For the computational grid patterns of the innermost region in Figure 3, the local effects of ocean tide loading is computed when the file containing amplitude and phase is imported. In this case, the innermost region would be defined as the area within the lower threshold of the near regions. The SRTM DEM is recommended to extract the local land–ocean boundary, and the grid size would be the same as that in near region 1. Moreover, the gravitational

part of Green's functions would be calculated by a tesseroid approximation [47].

### 2.5 Loading gravity effects

As shown in Figure 2, our software can export the calculation results of amplitude and phase of the loading gravity effects to the selected file. Based on the International Earth Rotation Service Conventions Note 36, the gravity change time-series can be further transformed by [48]:

$$G_c(\varphi, \lambda, t) = \sum_{p=0}^{n} f_p L_p \cos\left(\omega_p t_i + \chi_p + \mu_p - \alpha_p\right) \quad (7)$$

where $L_p$ and $\alpha_p$ are the amplitude and phase of the pth tidal constituent, respectively, t is the time at ith epoch, $f_p$ and $\mu_p$ are the nodal corrections. For a given observation epoch and sampling interval, the results calculated by formula (7) can be used as corrections of terrestrial gravity measurements.

## 3 Results and analysis

### 3.1 Verification of computation results

Our computation results were verified using the Bos–Scherneck, which has been recommended as the ocean tide loading provider by the International Geodynamics and Earth Tide Service [49]. The results of ocean tide loading from Bos–Scherneck were also derived from ocean tide models using an integration over all global tidal masses using Green's functions for the Gutenberg–Bullen or STW105 Earth model, providing site-specific amplitudes and phases of loading gravity extracted for the 11 main constituents for each ocean tide model.

As shown in Figure 1, we analyzed the results of ocean tide loading at five gravity stations along the coast of the Chinese mainland, approximately 60, 10, 70, 25, and 110 km from the coastline. Here, the height datum of the station elevation is the mean sea level. The ocean tide model and Green's functions were selected as Fes2004 and Gutenberg–Bullen, respectively. As shown in Table 1, the amplitudes and related phases of loading gravity effects for eight main tidal constituents were given at the five gravity stations. The stations, especially those close to the coastline, would be strongly affected by ocean tide loading, and the maximum amplitude can reach 6.02 μGal at Pingtan station. For the difference in amplitude between GOTL and Bos–Scherneck, the larger values are at Pingtan and Qingdao stations, reaching 0.17 μGal. In addition to these two stations, the difference in amplitude was within 0.03 μGal. The difference between the computational results of the two software programs is related to the coastline data and the convolution integration method, especially in the coastline representation [50–52]. The overall difference in phase for K2 waves was relatively large, reaching 17.1°. This is most likely due to its small magnitude making it more sensitive to the above effects.

Figure 4 shows the predicted gravity time series due to ocean tide loading derived from GOTL and Bos–Scherneck. The sampling time interval and reference time were selected as 1 min and UTC, respectively. The maximum peak to peak of the gravity time series can reach approximately 7.00, 20.56, 9.14, 5.53, and 2.93 μGal at Qiongzhong, Pingtan, Sheshan, Qingdao, and Jixian stations, respectively. However, these two software programs gave relatively consistent results during August 2020. The difference in the two predicted time series was within 0.25, 0.42, 0.21, 0.29, and 0.14 μGal at Qiongzhong, Pingtan, Sheshan, Qingdao, and Jixian stations, respectively, and the related correlation coefficients are all approximately 1.0. The above results show that the software in our study can accurately describe the variation characteristics of the gravitational effects of the ocean tide load in time and space.

### 3.2 Comparison of ocean tide models

The quality of the ocean tide model is one of the main factors affecting the accuracy of ocean tide loading effects. To evaluate the influence of the ocean tide model on the loading gravity effects, we compared the results obtained for the Fes2004 model with the results for the FES2014b and TPXO9_Atlas models. The Gutenberg–Bullen Green's function was selected. Table 2 shows the computational results of loading gravity effects for the three ocean tide models from GOTL. The results given by these three ocean tide models were quite different. Compared with the Fes2004 model, the maximum difference of amplitude and phase for FES2014b can reach 0.35 μGal and 50.0°, respectively. Furthermore, the maximum difference of amplitude and phase for TPXO9_Atlas can reach 0.35 μGal and 48.4°, respectively. The results also showed that the differences were larger at Qingdao and Sheshan stations, which were closer to the coast and had a more complex coastline. The above results demonstrated that the loading gravity effects were sensitive to the quality of the ocean tide model.

The spatial resolutions of FES2004, FES2014b, and TPXO9_Atlas used in our study were 1/8, 1/16, and 1/30°,

**Table 1:** The amplitudes and related phases of loading gravity effects from GOTL and Bos–Scherneck.

| Station | Harmonic | GOTL | | Bos-Scherneck | | Difference | |
|---|---|---|---|---|---|---|---|
| | | Amplitude (μGal) | Phase (degree) | Amplitude (μGal) | Phase (degree) | Amplitude (μGal) | Phase (degree) |
| Qiongzhong (109.8°E, 19.0°N) | M2 | 1.08 | −150.8 | 1.09 | −147.6 | −0.01 | −3.2 |
| | S2 | 0.30 | −134.8 | 0.27 | −128.4 | 0.03 | −6.4 |
| | N2 | 0.23 | −172.5 | 0.20 | −169.2 | 0.03 | −3.3 |
| | K2 | 0.07 | −122.8 | 0.09 | −108.3 | −0.02 | −14.5 |
| | K1 | 1.35 | 18.8 | 1.37 | 19.4 | −0.02 | −0.6 |
| | O1 | 1.43 | −10.6 | 1.46 | −7.9 | −0.03 | −2.7 |
| | P1 | 0.51 | 25.4 | 0.51 | 26.5 | 0.00 | −1.1 |
| | Q1 | 0.28 | −24.5 | 0.31 | −17.9 | −0.03 | −6.6 |
| Pingtan (119.8°E, 25.5°N) | M2 | 6.02 | −121.0 | 6.07 | −120.0 | −0.05 | −1.0 |
| | S2 | 1.32 | −103.9 | 1.31 | −101.7 | 0.01 | −2.2 |
| | N2 | 1.09 | −154.0 | 1.08 | −152.9 | 0.01 | −1.1 |
| | K2 | 0.36 | −110.6 | 0.22 | −117.0 | 0.14 | 6.4 |
| | K1 | 2.14 | −65.4 | 2.22 | −64.0 | −0.08 | −1.4 |
| | O1 | 2.04 | −84.1 | 2.09 | −82.9 | −0.05 | −1.2 |
| | P1 | 0.71 | −62.9 | 0.74 | −61.9 | −0.03 | −1.0 |
| | Q1 | 0.44 | −99.4 | 0.43 | −95.3 | 0.01 | −4.1 |
| Sheshan (121.2°E, 31.3°N) | M2 | 1.77 | −149.2 | 1.80 | −150.6 | −0.03 | 1.4 |
| | S2 | 0.47 | −155.1 | 0.45 | −156.2 | 0.02 | 1.1 |
| | N2 | 0.41 | −170.4 | 0.40 | −171.1 | 0.01 | 0.7 |
| | K2 | 0.11 | −152.6 | 0.08 | −162.9 | 0.03 | 10.3 |
| | K1 | 1.49 | −97.7 | 1.52 | −95.7 | −0.03 | −2.0 |
| | O1 | 1.19 | −112.0 | 1.21 | −110.6 | −0.02 | −1.4 |
| | P1 | 0.47 | −95.5 | 0.49 | −93.6 | −0.02 | −1.9 |
| | Q1 | 0.27 | −126.9 | 0.25 | −122.8 | 0.02 | −4.1 |
| Qingdao (120.3°E, 36.1°N) | M2 | 1.74 | 98.4 | 1.91 | 101.2 | −0.17 | −2.8 |
| | S2 | 0.50 | 143.8 | 0.53 | 146.4 | −0.03 | −2.6 |
| | N2 | 0.28 | 105.3 | 0.30 | 103.1 | −0.02 | 2.2 |
| | K2 | 0.14 | 128.2 | 0.13 | 126.5 | 0.01 | 1.7 |
| | K1 | 0.38 | −90.5 | 0.38 | −85.7 | 0.00 | −4.8 |
| | O1 | 0.57 | −84.9 | 0.57 | −82.0 | 0.00 | −2.9 |
| | P1 | 0.13 | −84.8 | 0.14 | −80.6 | −0.01 | −4.2 |
| | Q1 | 0.13 | −125.4 | 0.11 | −116.4 | 0.02 | −9.0 |
| Jixian (117.5°E, 40.1°N) | M2 | 0.28 | 128.2 | 0.31 | 123.5 | −0.03 | 4.7 |
| | S2 | 0.22 | 121.4 | 0.22 | 114.9 | 0.00 | 6.5 |
| | N2 | 0.11 | 153.3 | 0.09 | 143.7 | 0.02 | 9.6 |
| | K2 | 0.06 | 130.8 | 0.05 | 113.7 | 0.01 | 17.1 |
| | K1 | 0.59 | −124.9 | 0.61 | −121.9 | −0.02 | −3.0 |
| | O1 | 0.50 | −135.9 | 0.51 | −135.2 | −0.01 | −0.7 |
| | P1 | 0.20 | −122.4 | 0.21 | −118.9 | −0.01 | −3.5 |
| | Q1 | 0.12 | −149.0 | 0.10 | −145.9 | 0.02 | −3.1 |

respectively. With the advantage of a longer altimeter time series, more tidal gauges, and a better assimilation scheme, the latest FES2014b and TPXO9_Atlas exceeded the quality and resolution of older FES2004 in the vast majority of regions [53, 54]. The TPXO9_Atlas model, which integrates thirty 1/30-degree regional tidal models, including for the Pacific Ocean, has significantly improved the quality in shallow waters and coastal seas [54]. As shown in Table 2, the difference in amplitude and phase between FES2014b and TPXO9_Atlas was within 0.12 μGal and 10.9°, respectively. The results demonstrate that loading gravity effects have been improved in accuracy with the development of the ocean tide models. Moreover, it is necessary to adopt a higher-precision regional ocean tidal

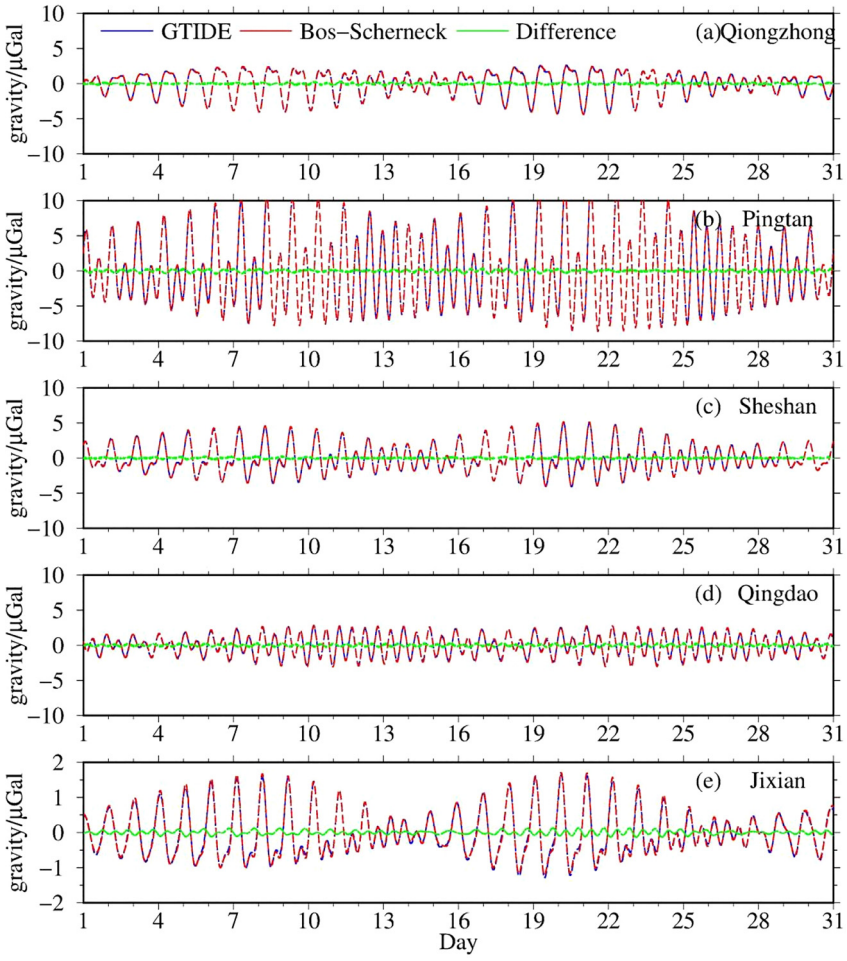


**Figure 4:** The gravity time series of ocean tide loading from GOTL (blue) and Bos–Scherneck (red) during August 2020.

model and tidal gauge data to improve the accuracy of ocean tide loading [55, 56].

## 3.3 Comparison of Green's functions

The Green's functions constitute another important factor affecting the accuracy of ocean tide loading effects. To evaluate the influence of Green's functions on the loading gravity effects, we compared the results obtained for the Gutenberg–Bullen with the results for the PREM and PREM-hard Earth models. Here, the ocean tide model was set as the FES2004 model. For these three Green's functions, the discrepancy in corresponding Earth models is mainly reflected in the crust and upper mantle. Compared with the two representative Gutenberg–Bullen and PREM Earth models, PREM-hard has been modified by the global-averaged Crust2.0, which improves the resolution of crustal elastic structure in depth [26].

Table 3 gives the amplitudes and related phases of loading gravity effects for the above three Green's functions from GOTL. Except for Pingtan and Qingdao stations, the difference in amplitude between Gutenberg–Bullen and PREM, PREM-hard was within 0.02 μGal, and the phase difference was within 2.9°. However, for the coastal Pingtan and Qingdao stations, the loading gravity effects were more sensitive to the Green's functions. The maximum amplitude difference between Gutenberg–Bullen and PREM can reach 0.23 and 0.02 μGal, respectively, and that between Gutenberg–Bullen and PREM-hard can reach 0.51 and 0.07 μGal, respectively. In practical application, we found that the differences in those three Green's functions were in the near field less than 1° from the observation station. For PREM-hard, the corresponding differences were more obvious in regions less than 0.1° (approximately 10 km) from the observation station. The distances from the Pingtan and Qingdao stations to the coastline were 10 and 25 km, respectively. Our results suggest that the influence of the Green's functions on loading gravity effects should be considered at coastal stations, especially for those less than 10 km from the coastline.

**Table 2:** The amplitudes and related phases of loading gravity effects for different ocean tide models from GOTL.

| Station | Harmonic | FES2004 | | FES2014 | | TPXO9_atlas | |
|---|---|---|---|---|---|---|---|
| | | Amplitude (μGal) | Phase (degree) | Amplitude (μGal) | Phase (degrees) | Amplitude (μGal) | Phase (degree) |
| Qiongzhong (109.8°E, 19.0°N) | M2 | 1.08 | −150.8 | 1.01 | −150.1 | 1.09 | −154.1 |
| | S2 | 0.30 | −134.8 | 0.29 | −120.5 | 0.31 | −129.6 |
| | N2 | 0.23 | −172.5 | 0.23 | −163.9 | 0.24 | −165.2 |
| | K2 | 0.07 | −122.8 | 0.11 | −129.3 | 0.10 | −124.9 |
| | K1 | 1.35 | 18.8 | 1.34 | 16.5 | 1.30 | 18.5 |
| | O1 | 1.43 | −10.6 | 1.29 | −8.5 | 1.30 | −7.9 |
| | P1 | 0.51 | 25.4 | 0.45 | 10.2 | 0.42 | 12.8 |
| | Q1 | 0.28 | −24.5 | 0.31 | −22.5 | 0.31 | −24.6 |
| Pingtan (119.8°E, 25.5°N) | M2 | 6.02 | −121.0 | 5.96 | −122.6 | 6.02 | −122.1 |
| | S2 | 1.32 | −103.9 | 1.50 | −93.6 | 1.47 | −95.6 |
| | N2 | 1.09 | −154.0 | 1.26 | −146.4 | 1.23 | −144.9 |
| | K2 | 0.36 | −110.6 | 0.43 | −101.0 | 0.45 | −102.2 |
| | K1 | 2.14 | −65.4 | 2.32 | −62.2 | 2.27 | −62.7 |
| | O1 | 2.04 | −84.1 | 2.04 | −86.7 | 2.08 | −85.0 |
| | P1 | 0.71 | −62.9 | 0.74 | −65.5 | 0.75 | −64.0 |
| | Q1 | 0.44 | −99.4 | 0.43 | −102.1 | 0.44 | −96.8 |
| Sheshan (121.2°E, 31.3°N) | M2 | 1.77 | −149.2 | 2.12 | −138.1 | 2.06 | −141.6 |
| | S2 | 0.47 | −155.1 | 0.70 | −105.1 | 0.63 | −106.7 |
| | N2 | 0.41 | −170.4 | 0.47 | −158.4 | 0.47 | −160.0 |
| | K2 | 0.11 | −152.6 | 0.22 | −118.6 | 0.21 | −120.1 |
| | K1 | 1.49 | −97.7 | 1.53 | −97.6 | 1.50 | −96.7 |
| | O1 | 1.19 | −112.0 | 1.18 | −116.3 | 1.18 | −113.0 |
| | P1 | 0.47 | −95.5 | 0.50 | −99.8 | 0.49 | −97.6 |
| | Q1 | 0.27 | −126.9 | 0.24 | −126.3 | 0.24 | −120.9 |
| Qingdao (120.3°E, 36.1°N) | M2 | 1.74 | 98.4 | 1.97 | 90.2 | 2.09 | 91.9 |
| | S2 | 0.50 | 143.8 | 0.73 | 112.9 | 0.73 | 117.1 |
| | N2 | 0.28 | 105.3 | 0.37 | 75.2 | 0.38 | 76.5 |
| | K2 | 0.14 | 128.2 | 0.22 | 110.9 | 0.18 | 116.9 |
| | K1 | 0.38 | −90.5 | 0.34 | −69.3 | 0.30 | −71.5 |
| | O1 | 0.57 | −84.9 | 0.55 | −82.0 | 0.56 | −78.7 |
| | P1 | 0.13 | −84.8 | 0.16 | −83.0 | 0.15 | −72.41 |
| | Q1 | 0.13 | −125.4 | 0.16 | −98.3 | 0.16 | −96.0 |
| Jixian (117.5°E, 40.1°N) | M2 | 0.28 | 128.2 | 0.38 | 117.3 | 0.41 | 123.9 |
| | S2 | 0.22 | 121.4 | 0.20 | 116.1 | 0.20 | 127.0 |
| | N2 | 0.11 | 153.3 | 0.09 | 142.3 | 0.09 | 143.4 |
| | K2 | 0.06 | 130.8 | 0.07 | 119.7 | 0.06 | 130.4 |
| | K1 | 0.59 | −124.9 | 0.60 | −125.9 | 0.59 | −126.0 |
| | O1 | 0.50 | −135.9 | 0.50 | −142.2 | 0.49 | −139.3 |
| | P1 | 0.20 | −122.4 | 0.20 | −128.0 | 0.19 | −122.0 |
| | Q1 | 0.12 | −149.0 | 0.11 | −149.7 | 0.11 | −140.3 |

# 4 Discussion

Using the high-precision coastline, ocean tide model, and Green's functions, a correction software for gravitational effects of ocean tide loading was developed and applied at five stations in the CEGN. As shown in Table 1, the reliability and applicability of the software were analyzed through comparison with the existing international software. With the exception of the coastal stations, the difference between the calculation results of the two software programs was relatively small. This indirectly proves that the coastline can affect the computational gravitational effects of ocean tide loading. Thus, it is

**Table 3:** The amplitudes and related phases of loading gravity effects for different Green's functions from GOTL.

| Station | Harmonic | Gutenberg-Bullen | | PREM | | PREM-hard | |
|---|---|---|---|---|---|---|---|
| | | Amplitude (μGal) | Phase (degree) | Amplitude (μGal) | Phase (degree) | Amplitude (μGal) | Phase (degree) |
| Qiongzhong (109.8°E, 19.0°N) | M2 | 1.08 | −150.8 | 1.08 | −150.8 | 1.08 | −150.1 |
| | S2 | 0.30 | −134.8 | 0.30 | −134.8 | 0.29 | −132.8 |
| | N2 | 0.23 | −172.5 | 0.23 | −172.5 | 0.22 | −171.6 |
| | K2 | 0.07 | −122.8 | 0.07 | −122.8 | 0.07 | −120.7 |
| | K1 | 1.35 | 18.8 | 1.35 | 18.8 | 1.37 | 17.9 |
| | O1 | 1.43 | −10.6 | 1.43 | −10.6 | 1.44 | −11.0 |
| | P1 | 0.51 | 25.4 | 0.51 | 25.4 | 0.51 | 24.3 |
| | Q1 | 0.28 | −24.5 | 0.28 | −24.5 | 0.29 | −23.4 |
| Pingtan (119.8°E, 25.5°N) | M2 | 6.02 | −121.0 | 5.79 | −121.9 | 5.51 | −123.1 |
| | S2 | 1.32 | −103.9 | 1.27 | −105.2 | 1.20 | −107.3 |
| | N2 | 1.09 | −154.0 | 1.05 | −154.8 | 1.01 | −156.1 |
| | K2 | 0.36 | −110.6 | 0.34 | −111.9 | 0.33 | −113.9 |
| | K1 | 2.14 | −65.4 | 2.13 | −65.2 | 2.09 | −65.4 |
| | O1 | 2.04 | −84.1 | 2.02 | −83.9 | 1.99 | −84.0 |
| | P1 | 0.71 | −62.9 | 0.71 | −62.9 | 0.69 | −63.1 |
| | Q1 | 0.44 | −99.4 | 0.43 | −98.1 | 0.42 | −98.2 |
| Sheshan (121.2°E, 31.3°N) | M2 | 1.77 | −149.2 | 1.78 | −149.9 | 1.78 | −150.2 |
| | S2 | 0.47 | −155.1 | 0.47 | −155.2 | 0.47 | −155.5 |
| | N2 | 0.41 | −170.4 | 0.40 | −170.7 | 0.40 | −170.9 |
| | K2 | 0.11 | −152.6 | 0.11 | −152.6 | 0.11 | −152.9 |
| | K1 | 1.49 | −97.7 | 1.49 | −96.8 | 1.50 | −96.8 |
| | O1 | 1.19 | −112.0 | 1.19 | −111.2 | 1.19 | −111.2 |
| | P1 | 0.47 | −95.5 | 0.48 | −94.7 | 0.48 | −94.7 |
| | Q1 | 0.27 | −126.9 | 0.26 | −125.1 | 0.26 | −125.1 |
| Qingdao (120.3°E, 36.1°N) | M2 | 1.74 | 98.4 | 1.74 | 99.1 | 1.67 | 99.2 |
| | S2 | 0.50 | 143.8 | 0.48 | 144.5 | 0.48 | 143.5 |
| | N2 | 0.28 | 105.3 | 0.28 | 104.2 | 0.27 | 104.7 |
| | K2 | 0.14 | 128.2 | 0.14 | 127.6 | 0.14 | 127.4 |
| | K1 | 0.38 | −90.5 | 0.40 | −87.9 | 0.41 | −88.4 |
| | O1 | 0.57 | −84.9 | 0.57 | −84.0 | 0.58 | −85.1 |
| | P1 | 0.13 | −84.8 | 0.14 | −82.9 | 0.14 | −83.7 |
| | Q1 | 0.13 | −125.4 | 0.12 | −121.6 | 0.12 | −122.1 |
| Jixian (117.5°E, 40.1°N) | M2 | 0.28 | 128.2 | 0.27 | 128.4 | 0.27 | 128.4 |
| | S2 | 0.22 | 121.4 | 0.21 | 119.1 | 0.21 | 119.1 |
| | N2 | 0.11 | 153.3 | 0.10 | 150.3 | 0.10 | 150.4 |
| | K2 | 0.06 | 130.8 | 0.05 | 128.2 | 0.05 | 128.3 |
| | K1 | 0.59 | −124.9 | 0.59 | −122.2 | 0.59 | −122.2 |
| | O1 | 0.50 | −135.9 | 0.49 | −134.1 | 0.49 | −134.1 |
| | P1 | 0.20 | −122.4 | 0.20 | −119.8 | 0.20 | −119.8 |
| | Q1 | 0.12 | −149.0 | 0.11 | −146.7 | 0.11 | −146.7 |

necessary to use a high-precision local coastline to improve the accuracy of ocean tide loading. In view of this, our software can further import a DEM with 90 m resolution, as shown in Figure 2, which was obtained by the SRTM. In this case, the coastline in the near regions would be extracted from SRTM DEM. The SRTM DEM would provide a high-precision ocean–land boundary and effectively improve the calculation accuracy of ocean tide loading.

As shown in Table 4, the amplitudes and related phases of loading gravity effects were computed from GSHHG and SRTM at two coastal stations. Here, the ocean tide model and Green's functions were set as FES2004 and Gutenberg–Bullen, respectively. For Pingtan station,

**Table 4:** The amplitudes and related phases of loading gravity effects from GSHHG and SRTM.

| Station | Harmonic | GSHHG | | SRTM | |
|---|---|---|---|---|---|
| | | Amplitude (μGal) | Phase (degree) | Amplitude (μGal) | Phase (degree) |
| Pingtan (119.8°E, 25.5°N) | M2 | 6.02 | −121.0 | 6.86 | −118.2 |
| | S2 | 1.32 | −103.9 | 1.52 | −98.8 |
| | N2 | 1.09 | −154.0 | 1.21 | −150.7 |
| | K2 | 0.36 | −110.6 | 0.41 | −105.8 |
| | K1 | 2.14 | −65.4 | 2.24 | −64.7 |
| | O1 | 2.04 | −84.1 | 2.14 | −83.7 |
| | P1 | 0.71 | −62.9 | 0.74 | −62.3 |
| | Q1 | 0.44 | −99.4 | 0.46 | −99.0 |
| Qingdao (120.3°E, 36.1°N) | M2 | 1.74 | 98.4 | 1.89 | 98.4 |
| | S2 | 0.50 | 143.8 | 0.52 | 146.2 |
| | N2 | 0.28 | 105.3 | 0.30 | 104.5 |
| | K2 | 0.14 | 128.2 | 0.16 | 131.3 |
| | K1 | 0.38 | −90.5 | 0.35 | −89.5 |
| | O1 | 0.57 | −84.9 | 0.56 | −82.9 |
| | P1 | 0.13 | −84.8 | 0.12 | −83.3 |
| | Q1 | 0.13 | −125.4 | 0.13 | −124.8 |

the maximum difference in amplitude and phase between GSHHG and SRTM can reach 0.84 μGal and 5.1°, respectively. For Qingdao station, the maximum difference in amplitude and phase between GSHHG and SRTM can reach 0.15 μGal and 3.1°, respectively. The calculation results of Pingtan station, which was closer to the coast, were more vulnerable to the influence of the coastline.

Table 2 shows that the global ocean tide model has a certain impact on the computational gravitational effects of ocean tide loading. The current ocean tide models were obtained from satellite altimetry or the assimilation of satellite altimetry. The accuracy of the global ocean tide model remains poor in certain coastal regions owing to three factors: (1) The model is greatly affected by the coastline and seabed topography, especially in bays, trenches, and shallow waters, because of the uncertainty of bathymetry, bottom friction and viscosity coefficients, and boundary conditions. (2) The model is greatly affected by the offshore marine environment where the quality of satellite altimetry is poor owing to the bad reflection signal. (3) The assimilation of tidal gauge records is insufficient [20–22]. Owing to the poor quality of the global ocean tide model in coastal regions, a more accurate local tidal model can be imported to replace the global ocean tide model in our software (as shown in Figure 2), which would improve the accuracy of global loading gravity effects [55, 56]. In addition, the local loading gravity effect is an important component affecting gravity observations [57–63]. Therefore, our software can import the local tidal gauge record to comprehensively improve the calculation accuracy of ocean tide loading.

Table 3 shows that the Green's functions have a certain impact on the computational gravitational effects of ocean tide loading at coastal stations. As shown in Figure 5, the values of Green's functions exhibited significant differences in the near-field (less than 1°) due to the discrepancies of physical parameters for the Earth model. For PREM-hard and PREM-soft, the crust structures of the PREM Earth model were composed by Crust 2.0, in which the outmost layer is composed of hard and soft sediments, respectively [21]. The discrepancies were larger for the Green's functions in the adjoining areas (especially those at

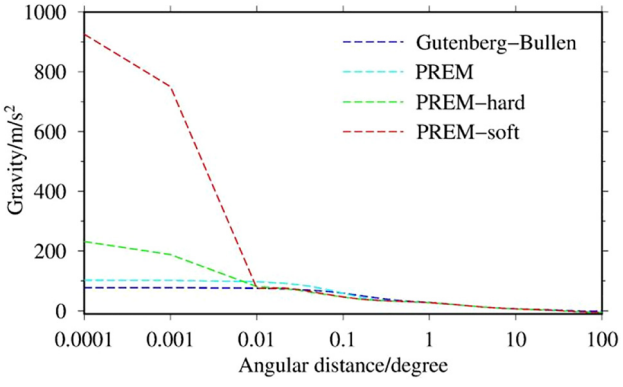


**Figure 5:** The gravity Green's functions for the Gutenberg–Bullen, PREM, PREM-hard, and PREM-soft earth models. Gravity is positive upwards and scaled by $10^{18}$, the radius of the earth, and the angular distance to the station. The surface mass of applied load is 1 kg.

less than 0.1°) among the Gutenberg–Bullen, PREM-hard, and PREM-soft. Hence, the results of ocean tide loading would have obvious differences in the near field. Therefore, it is necessary to use PREM-hard or PREM-soft Green's functions to improve the accuracy of local loading gravity effects, especially for those stations less than 0.1° from the coastline.

# 5 Conclusions

In this study, we developed a correction software, GOTL, for the gravitational effects of ocean tide loading. In the modeling process, we divided the ocean tide contributions into five parts: innermost, near, middle, and far regions. The effects of three-dimensional station coordinates, computational grid patterns, ocean tide models, Green's functions, coastline, and local tide gauge are all considered in the programming process. Compared with the existing software, our contributions are mainly reflected in the following four points. (1) During software design, the advantages of matrix operation and the graphical user interface were fully utilized. All the key parameters during calculation can be set in the graphical user interface, and the loading amplitudes, phases, and corresponding predicted gravity time series could be given together. This can effectively increase the operability and practicability of the software. (2) Several of the latest ocean tide models and Green's functions have been added to the software. (3) In the innermost region, the local effects model has been added to the software by further importing the tidal gauge record, and the corresponding gravitational part of Green's functions would be calculated using a tesseroid approximation. (4) In the innermost and near regions, a high-precision ocean–land boundary with 90 m resolution can be extracted from SRTM DEM, which can improve the calculation accuracy of ocean tide loading, especially in some regions with complex coastlines. The results in our study indicate that the GOTL software can accurately describe the variation characteristics of gravitational effects of ocean tide loading in space and time.

At present, a gravity observation network composed of relative gravity and absolute gravity has been installed along the coast of the Chinese mainland. Based on the results of our study, the impact of ocean tide loading should be seriously considered in certain coastal and island regions. In addition, our results show that the correction of loading gravity effects are sensitive to the accuracy of the coastline, ocean tide model, and internal structure of the Earth. Based on the higher-precision local ocean tide model, tidal gauge record, coastline, and Green's functions modified by refined crustal structure, our software would improve the accuracy of gravitational effects of loading effects at stations in the CEGN.

**Acknowledgments:** We acknowledge the AVISO, CEOAS, NAOJ, DGFI, DTU, and CSR for providing the ocean tide models and NOAA for providing GSHHG data. We also acknowledge Bos–Scherneck for providing computational results of ocean tide loading, Wang H L for providing computational results of Green's functions for PREM, iasp91, ak135, and modified PREM-soft, PREM-hard. CGIAR for providing SRTM DEM data. The figures are generated using the Generic Mapping Tools software.

**Author contributions:** CDZ contributed to the design of the study, data processing, analysis of results, and manuscript writing. LQP contributed to reviewing and editing the manuscript. DDS, JLH and JWL contributed to data processing.

**Research funding:** This study was funded by The Science and Technology Innovation Fund of the First Monitoring and Application Center, CEA (NO. FMC2022001), National Key Research and Development Program of China (NO. 2018YFC1503606), and The Science for Earthquake Resilience (No. XH22016YA, XH22017YA).

**Conflict of interest:** All the authors declare no competing financial and non-financial interests.

# References

1. Chen YT, Gu HD, Xun LZ. Variations of gravity before and after the Haicheng earthquake, 1975, and the Tangshan earthquake, 1976. Phys Earth Planet In 1979;18:330–8.
2. Li RH, Huang JL, Li H, Chen DS. The mechanism of regional gravity changes before and after the Tangshan earthquake. Acta Seismol Sin 1997;10:497–500.
3. Li H, Shen CY, Sun SA, Wang XQ, Xiang AM, Liu SM. Dynamic gravity change in recent years in China continent. J Geodesy Geodyn 2009;29:1–10.
4. Zhu YQ, Liu F, Zhang GQ, Xu Y. Development and prospect of mobile gravity monitoring and earthquake forecasting in recent ten years in China. J Geodesy Geodyn 2019;10: 485–91.
5. Shen CC, Zhu YQ, Hu MZ, Tan HB, Hao HT, Wei J, et al. Time-varying gravity field monitoring and strong earthquake prediction on the Chinese mainland. Earthq Res China 2020;36:729–43.
6. Crossley D, Hinderer J, Riccardi U. The measurement of surface gravity. Rep Prog Phys 2013;76:046101.
7. Van Camp M, de Viron O, Watlet A, Meurers B, Francis O, Caudron C. Geophysics from terrestrial time-variable gravity measurements. Rev Geophys 2017;55:938–92.
8. Farrell WE. Deformation of the Earth by surface loads. Rev Geophys 1972;10:761–97.

9. Schwiderski EW. Ocean tides, part I: global ocean tidal equations. Mar Geodes 1980;3:161–217.
10. Schwiderski EW. Ocean tides, part II: a hydrodynamical interpolation model. Mar Geodes 1980;3:219–55.
11. Lyard F, Lefevre F, Letellier T, Francis O. Modelling the global ocean tides: modern insights from FES2004. Ocean Dynam 2006;56:394–415.
12. Eanes R. The CSR 3.0 global ocean tide model, center for space research. Austin, Texas: Technical Memorandum; 1995, 95.
13. Ray RD. A global ocean tide model from TOPEX/POSEIDON altimetry: GOT99. 2. Greenbelt, MD: National Aeronautics and Space Administration, Goddard Space Flight Center; 1999.
14. Matsumoto K, Takanezawa T, Ooe M. Ocean tide models developed by assimilating TOPEX/POSEIDON altimeter data into hydrodynamical model: a global model and a regional model around Japan. J Oceanogr 2000;56:567–81.
15. Egbert GD, Erofeeva SY. Efficient inverse modeling of barotropic ocean tides. J Atmos Ocean Technol 2002;19:183–204.
16. Savcenko R, Bosch W. EOT11a-empirical ocean tide model from multi-mission satellite altimetry. München: Deutsches Geodätisches Forschungsinstitut; 2012.
17. Cheng Y, Andersen OB. Improvement in global ocean tide model in shallow water regions. Poster 2010;45:1–68.
18. Fok HS. Ocean tides modeling using satellite altimetry. Columbus: The Ohio State University; 2012.
19. Taguchi E, Stammer D, Zahel W. Inferring deep ocean tidal energy dissipation from the global high-resolution data-assimilative HAMTIDE model. J Geophys Res: Oceans 2014;119:4573–92.
20. Shum CK, Woodworth PL, Andersen OB, Egbert GD, Francis O, King C, et al. Accuracy assessment of recent ocean tide models. J Geophys Res: Oceans 1997;102:25173–94.
21. Stammer D, Ray RD, Andersen OB, Arbic BK, Bosch W, Carrère L, et al. Accuracy assessment of global barotropic ocean tide models. Rev Geophys 2014;52:243–82.
22. Cheng Y, Andersen OB. Multimission empirical ocean tide modeling for shallow waters and polar seas. J Geophys Res: Oceans 2011;116:1–11.
23. Longman IM. Computation of Love numbers and load deformation coefficients for a model Earth. Geophys J Int 1966;11:133–7.
24. Longman IMA. Green's function for determining the deformation of the Earth under surface mass loads: 2. Computations and numerical results. J Geophys Res 1963;68:485–96.
25. Dziewonski AM, Anderson DL. Preliminary reference earth model. Phys Earth Planet In 1981;25:297–356.
26. Wang HS, Xiang LW, Jia LL, Jiang L, Wang Z, Hu B, et al. Load Love numbers and Green's functions for elastic Earth models PREM, iasp91, ak135, and modified models with refined crustal structure from Crust 2.0. Comput Geosci 2012;49:190–9.
27. Agnew DC. SPOTL: some programs for ocean-tide loading. SIO Ref. Ser. 96–8. Calif: Scripps Instit of Oceanogr, La Jolla; 1996:35 p.
28. Agnew DC. NLOADF: a program for computing ocean-tide loading. J Geophys Res Solid Earth 1997;102:5109–10.
29. Agnew DC. SPOTL: some programs for ocean-tide loading (SIO Technical Report). Los Angeles, California: Scripps Institution of Oceanography. University of California; 2012.
30. Scherneck HG, Bos M. Ocean tide loading provider. Available from: http://holt.oso.chalmers.se/loading/.
31. Matsumoto K, Sato T, Takanezawa T, Ooe M. GOTIC2: a program for computation of oceanic tidal loading effect. J Geodetic Soc Jpn 2001;47:243–8.
32. Hwang C, Huang JF. SGOTL: a computer program for modeling high-resolution, height-dependent gravity effect of ocean tide loading. Terr Atmos Ocean Sci 2012;23:219–29.
33. Martens HR, Rivera L, LoadDef SM. A Python-based toolkit to model elastic deformation caused by surface mass loading on spherically symmetric bodies. Earth Space Sci 2019;6: 311–23.
34. Pagiatakis SD. The response of a realistic earth to ocean tide loading. Geophys J Int 1990;103:541–60.
35. Bos MS, Scherneck HG. Computation of Green's functions for ocean tide loading. Sciences of Geodesy-II. Berlin, Heidelberg: Springer; 2013:1–52 pp.
36. Goad CC. Gravimetric tidal loading computed from integrated Green's functions. J Geophys Res Solid Earth 1980;85:2679–83.
37. Francis O, Mazzega P. Global charts of ocean tide loading effects. J Geophys Res: Oceans 1990;95:11411–24.
38. Wessel P, Smith WH. A global, self-consistent, hierarchical, high-resolution shoreline database. J Geophys Res Solid Earth 1996;101:8741–3.
39. Farr TG, Kobrick M. Shuttle radar topography mission produces a wealth of data. Eos, Trans Am Geophys Union 2000;81:583–5.
40. Farr TG, Rosen PA, Caro E, Crippen R, Duren R, Hensley S, et al. The shuttle radar topography mission. Rev Geophys 2007;45:1–43.
41. Agnew DC. Conservation of mass in tidal loading computations. Geophys J Int 1983;72:321–5.
42. Dickman SR. Experiments in tidal mass conservation. Geophys J Int 1990;102:257–62.
43. Zhou MS, Liu X, Yuan JJ, Jin X, Niu Y, Guo J, et al. Seasonal variation of GPS-derived the principal ocean tidal constituents' loading displacement parameters based on moving harmonic analysis in Hong Kong. Rem Sens 2021; 13:279.
44. Turcotte DL. Geophysical geodesy: the slow deformations of the earth. Science 1989;244:995–6.
45. Okubo S, Saito M. Partial derivative of Love numbers. Bull Geod 1983;57:167–79.
46. Mikolaj M, Meurers B, Güntner A. Modelling of global mass effects in hydrology, atmosphere and oceans on surface gravity. Comput Geosci 2016;93:12–20.
47. Heck B, Seitz K. A comparison of the tesseroid, prism and point-mass approaches for mass reductions in gravity field modelling. J Geodes 2007;81:121–36.
48. Petit G, Luzum B. IERS technical note no. 36. Frankfurt am Main: Verlag des Bundesamts für Kartographie und Geodäsie; 2010. 179 p.

49. International Geodynamics and Earth Tide Service. Available from: http://igets.u-strasbg.fr/soft_and_tool.php.
50. Bos MS, Baker TF. An estimate of the errors in gravity ocean tide loading computations. J Geodes 2005;79: 50–63.
51. Bos MS, Baker TF, Røthing K, Plag HP. Testing ocean tide models in the Nordic seas with tidal gravity observations. Geophys J Int 2002;150:687–94.
52. Zhou J, Hwang C, Sun H, Xu J, Zhang W, Kao R, et al. Precise determination of ocean tide loading gravity effect for absolute gravity stations in coastal area of China: effects of land–sea boundary and station coordinate. J Geodyn 2013;68:29–36.
53. Lyard FH, Allain DJ, Cancet M, Carrère L, Picot N. FES2014 global ocean tide atlas: design and performance. Ocean Sci 2021;17:615–49.
54. OSU TPXO tide models. Available from: https://www.tpxo.net/home.
55. Lambert A, Pagiatakis SD, Billyard AP, Dragert H. Improved ocean tide loading corrections for gravity and displacement: Canada and northern United States. J Geophys Res Solid Earth 1998;103:30231–44.
56. Goring DG, Walters RA. Ocean-tide loading and Earth tides around New Zealand. N Z J Mar Freshw Res 2002;36:299–309.
57. Yamamoto K, Ishihara K, Okubo S, Araya A. Accurate evaluation of ocean tide loading effects for gravity in nearshore region: the FG5 measurements at Sakurajima volcano in Kagoshima Bay, Japan. Geophys Res Lett 2001;28:1807–10.
58. Sun HP, Hsu HT, Jentzsch G, Xu JQ. Tidal gravity observations obtained with a superconducting gravimeter at Wuhan/China and its application to geodynamics. J Geodyn 2002;33:187–98.
59. Boy JP, Llubes M, Ray R, Hinderer J, Florsch N, Rosat S, et al. Non-linear oceanic tides observed by superconducting gravimeters in Europe. J Geodyn 2004;38:391–405.
60. Khan SA, Høyer JL. Shallow-water loading tides in Japan from superconducting gravimetry. J Geodes 2004;78: 245–50.
61. Neumeyer J, del Pino J, Dierks O, Sun HP, Pflug H. Improvement of ocean loading correction on gravity data with additional tide gauge measurements. J Geodyn 2005;40:104–11.
62. Lysaker DI, Breili K, Pettersen BR. The gravitational effect of ocean tide loading at high latitude coastal stations in Norway. J Geodes 2008;82:569–83.
63. Goto H, Sugihara M, Nishi Y, Ikeda H. Simultaneous gravity measurements using two superconducting gravimeters to observe temporal gravity changes below the nm s–2 level: ocean tide loading differences at different distances from the coast. Geophys J Int 2021;227:1591–601.


**Supplementary Material:** The online version of this article offers supplementary material (https://doi.org/10.1515/jag-2022-0023).